Temperature Sensing and In Vivo Imaging by Molybdenum Sensitized Visible Upconversion Luminescence of Rare-Earth Oxides

6 AUTHORS, INCLUDING:

Zhipeng Li

Capital Normal University

45 PUBLICATIONS **1,622** CITATIONS

Temperature Sensing and In Vivo Imaging by Molybdenum Sensitized Visible Upconversion Luminescence of Rare-Earth Oxides

Bin Dong,* Baosheng Cao, Yangyang He, Zhuang Liu, Zhipeng Li,* and Zhiqing Feng

Since the upconversion (UC) luminescence of rare-earth (RE) ions was discovered by Auzel in the mid-1960s,[1] it has received much attention in the fields of physics, chemistry, material science and life science because of their broad potential applications–e.g. color display, optoelectronics, sensor technology, laser cooling and in vivo imaging.[2] Discovered more than four decades ago, Er-Yb and Tm-Yb systems remain the key constituents for the majority of UC materials for blue, green, and red UC luminescence. In these systems, Yb with a larger absorption cross section at near infrared (NIR) acts as a photosensitizer to overcome the difficulty associated with the rather smaller absorption cross section of Er or Tm (Er(Tm)) due to the dipole-forbidden nature of intra-4f transitions.[1,3] The NIR photon energy is transferred efficiently from Yb to Er(Tm) ions. The upconversion occurs when the subsequent energy transfer (ET) promote electrons of Er(Tm) ions to high-lying energy levels whose radiative decay leads to UC emission of higher photon energy. However, due to effective coupling to the lattice vibrations of the host materials, most of the intermediate state excitations relax quite rapidly to lower lying levels, significantly hampering the UC efficiency (called the phonon quenching effect).[4] Hence, many recent studies of increasing the efficiency of UC luminescence focus on reducing the electron-phonon coupling using a range of different host materials. Among the UC materials, Er(Tm)-Yb co-doped fluorides are considered to be the most efficient host materials for green/blue UC luminescence due to the relatively low lattice phonon energy.[5] More recently, much attention has been focused on the size/shape/phase-controlled synthesis, and the potential application in bio-imaging of the Er(Tm)-Yb:NaYF$_4$ nanocrystals.[6] However, the UC efficiency of RE-oxide materials is still low because of the corresponding high phonon energies, which greatly hamper their applicability in a variety of areas such as optical temperature sensing, bio-imaging, transparent ceramics, laser crystal, and etc.[7] Thus, developing an alternative strategy to overcome the phonon quenching effect in RE-oxide based UC luminescent materials is of paramount importance in order to realize the large potential applications described above. The spectroscopic properties of transition mental (TM) ions are very sensitive to environment because of the exposure of d electrons, which increase their potential of tuning excited state properties to match the acceptor ions. Thus, the new potential enhancer of UC luminescence and novel cooperative NIR to visible UC processes are expected by using TM ions as sensitizer for RE ions.

Recently, we observed the intense green UC luminescence of Er-Mo:Yb$_2$Ti$_2$O$_7$, and preliminarily explored a possibility for optical thermometry.[8] Here, we investigate Er-Yb-Mo and Tm-Yb-Mo systems in oxidic matrix materials and have discovered an extraordinary enhancement of green and blue UC efficiency–a four orders of magnitude enhancement relative to the Er-Yb and Tm-Yb oxides without Mo doping. Our study further revealed that this extraordinary UC efficiency results from a novel ET pathway which entails a strong ground state absorption of Yb ions and the excited state absorption of Yb^{3+}-MoO$_4^{2-}$ dimers, followed by an effective energy transfer to the high energy state of Er(Tm) ions. Such an energy transfer process partly avoids the nonradiative decay processes happened at the lower energy levels of Er(Tm) ions, thus increasing the UC luminescence efficiency. Equally important are the exceptional material properties of these oxides, which significantly extend their scope of practical applications, such as temperature sensing and in vivo imaging.

The oxidic matrix materials co-doped with Er(Tm)-Yb-Mo ions under investigation are Al$_2$O$_3$, TiO$_2$, Gd$_2$O$_3$, and Yb$_3$Al$_5$O$_{12}$ (YbAG). All of these oxide materials with Er(Tm)-Yb-Mo co-doping show a similar high efficiency of UC luminescence. Here we concentrate on YbAG for detailed structural and optical spectroscopic analysis since YbAG offers a perfect single phase crystal structure in which every doped RE ion has Yb^{3+} as the nearest neighbor, so the effect of the Yb-Er and Yb-Tm interactions on the behavior of Er^{3+} and Tm^{3+} is expected to be strong.[9] **Figure 1**a shows XRD patterns taken from Er(Tm):YbAG and Er(Tm)-Mo:YbAG nanocrystals. All diffraction peaks can be well indexed following a cubic cell with a space group of Ia-3d,

Prof. B. Dong, B. S. Cao, Dr. Y. Y. He, Z. Q. Feng
Liaoning Key Lab of Optoelectronic Films & Materials
School of Physics and Materials Engineering
Dalian Nationalities University
Dalian, 116600, China
E-mail: dong@dlnu.edu.cn
Prof. Z. P. Li
Beijing Key Laboratory of Nano-Photonics and Nano-Structure
Department of Physics
Capital Normal University
Beijing, 100048, China
E-mail: zpli@cnu.edu.cn
Prof. Z. Liu
Functional Nano & Soft Materials Laboratory and Jiangsu Key Laboratory
for Carbon-Based Functional Materials & Devices
Soochow University
Suzhou, 215123, China
Dr. Y. Y. He
Faculty of Physics
University Duisburg-Essen
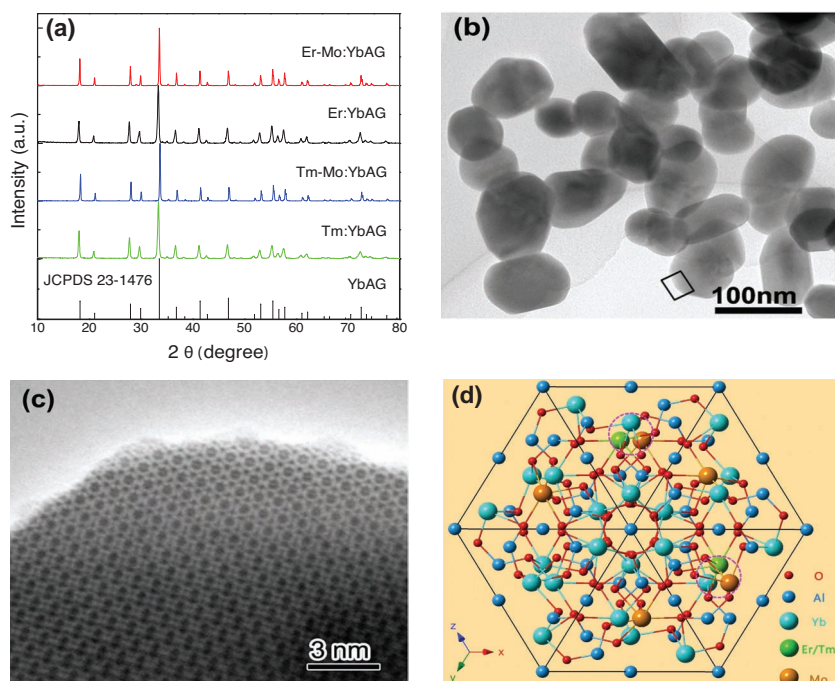Duisburg, 47057, Germany

COMMUNICATION

Figure 1. XRD patterns, TEM analysis and structural model of RE oxide nanoparticles. a) XRD patterns for Er(Tm):YbAG and Er(Tm)-Mo:YbAG samples. b) Typical TEM image of the Er-Mo:YbAG sample. c) HRTEM image from the square-enclosed region in (b). d) Structural model of the doped YbAG crystal projected along the [111] direction, the Mo and Er(Tm) cations are randomly distributed in the Yb sites (24c), the formed Yb-Mo-Er(Tm) cation functional cluster are indicated by dashed circles.

in good agreement with previous measurements of bulk YbAG as in the JCPDS No. 23-1476. This result suggests that the RE dopants occupy the chemical substitutional sites. Based on the Scherrer's equation, the calculated average crystal size of Er(Tm)-YbAG nanocrystals slightly increased with Mo addition, but no obvious change was observed due to the non-uniform grain sizes (Supporting information). A typical transmission electron microscope (TEM) image of Er-Mo-YbAG nanocrystals is given in Figure 1b. It can be seen that the Er(Tm)-Mo:YbAG nanocrystals have an average particle size ranging from 40 to 80 nm. Figure 1c is a high-resolution TEM image taken along the [111] zone-axis direction, indicating that the as-made samples are well crystallized.

$Yb_3Al_5O_{12}$ has a cubic unit cell with a lattice constant of $a = 11.9386$ Å, and a space group of Ia-3d.[10] There are two Al sites (the 16a octahedral site and the 24d tetrahedral site) and one unique Yb site (24c) in the ideal crystal structure. The $Yb_3Al_5O_{12}$ crystal offers, in principle, a single substitutional site for tri-valent RE^{3+} active ions, the dodecahedral 24c site normally occupied by Yb^{3+}, where no charge compensation is needed for substitution. In the doped crystals, Er and Yb cations are about 3.655 Å apart from each other.[10] The experimental data above (XRD and TEM) also suggest that Mo substitutes for the tri-valent Yb^{3+} ions too. This is indeed confirmed by our state-of-the-art first-principles modeling based on density functional theory. Accurate first-principles calculations show that configurations with both Er and Mo occupying Yb sites have a total energy ~1.8 eV lower than those configurations with

Mo occupying the Al site. This finding holds even for situations where the neighboring oxygen vacancies are involved. Figure 1d schematically shows the structural model obtained for the doped $Yb_3Al_5O_{12}$ crystal projected along the [111] direction; in this model, the Mo and Er(Tm) cations are randomly distributed in the Yb sites (24c). Also the units marked with dashed circles are the formed Yb-Mo-Er(Tm) cation clusters which act as efficient UC luminescence centers as discussed below.

UC emissions of Er(Tm)-Yb-Mo system in these oxides are much more efficient than the Er(Tm)-Yb system without Mo co-doping. In **Figure 2**a, the green and red UC emissions originating from the transitions of $^2H_{11/2}$, $^4S_{3/2} \rightarrow ^4I_{15/2}$ and $^4F_{9/2} \rightarrow ^4I_{15/2}$ were obtained for the Er-Mo and Er-doped samples, respectively. Compared with the Er:YbAG without Mo co-doping, the green UC luminescence of Er-Mo:YbAG enhanced by a factor of ~0.6×10^4, while the red UC luminescence increased by only ~30 times. For the Tm doped samples, the $^1G_4 \rightarrow ^3H_6$ transitions resulted in blue UC luminescence, $^1G_4 \rightarrow ^3F_4$ and $^3F_2 \rightarrow ^3H_6$ transitions caused red UC luminescence. The blue UC luminescence of Tm-Mo:YbAG in Figure 2b increased astonishingly about 1×10^4 times than that of Tm:YbAG, while $^3F_2 \rightarrow ^3H_6$ transitions of Tm-Mo:YbAG in red were totally immerse in the spectral background as shown in Figure 2b. Such intense blue UC luminescence overwhelmed the second harmonics (488 nm) of the laser line as indicated in Figure 2b. The intense green/blue UC luminescence can be easily observed with naked eyes, even at a pump power of ~30 mW cm^{-2} of 976 nm laser. The quantum yields of samples were shown in **Table 1**. To the best of our knowledge, the quantum yields of Er-Mo:YbAG (green: ~0.2%), and Tm-Mo:YbAG (blue: ~0.18%) are more efficient than the UC in any other rare-earth oxides, and are comparable to those of the Er-Yb:NaYF$_4$ nanocrystals[11] (Supporting information). It is worth to note that when Mo is replaced by W, a great enhancement of green UC luminescence is also observed in Er-W:YbAG nanocrystals (Supporting information).

The dependence of UC luminescence intensity upon the pump power P_{pump} sheds further light onto the underlying mechanism (**Figure 3**).[12] For green Er^{3+} UC emissions ($^2H_{11/2} \rightarrow ^4I_{15/2}$), the power law exponents for Er:YbAG and Er-Mo:YbAG systems are 1.72 and 1.86, respectively, indicating a two-photon process for both systems. For the blue Tm^{3+} UC emissions ($^1G_4 \rightarrow ^3H_6$), the Tm:YbAG sample shows an exponent of 2.83 indicating a three photon process for UC, while for Tm-Mo:YbAG, an exponent of 1.97 is observed, implying a two-photon process. The conclusion that UC blue emission is a two-photon process in Tm-Mo:YbAG is particularly intriguing since the energy of the emitted photons is more than twice of the excitation photons. Below we discuss the underlying mechanisms for this extraordinary UC efficiency.
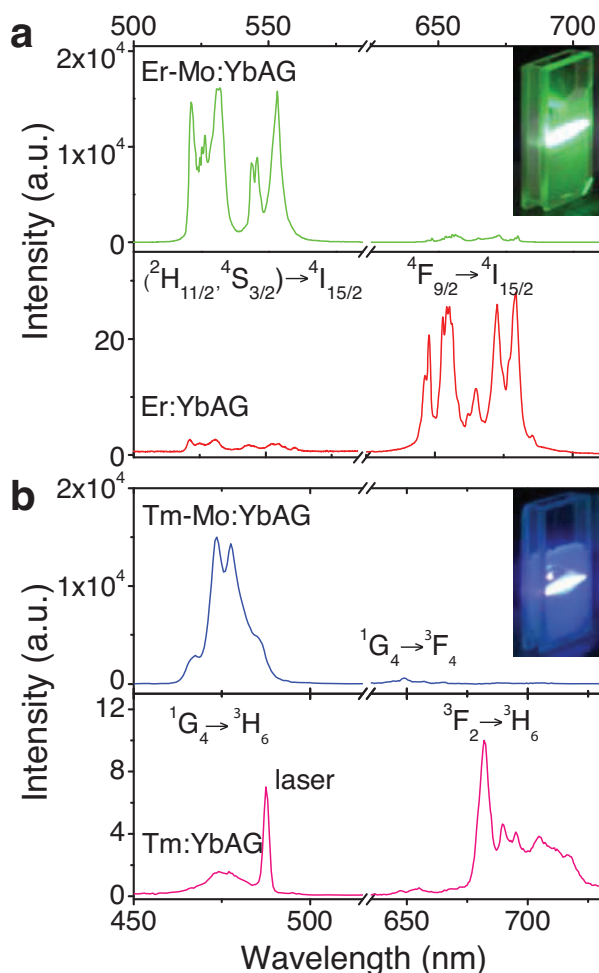
Figure 3. UC emission intensity versus the pump power P_{pump}.

Figure 2. The UC emissions spectra of the samples. a) Emissions from Er:YbAG and Er-Mo:YbAG. b) Emissions from Tm:YbAG and Tm-Mo:YbAG. The insets show color images of strong UC luminescence of RE oxides with Mo co-doping.

Figure 4a shows the UC mechanism for Er(Tm)-Yb systems where sequential sensitization and relaxation processes are responsible for the population of $^2H_{11/2}$, $^4S_{3/2}$ and $^4F_{9/2}$ levels of Er^{3+}, and $^1G_4$ and $^3F_2$ levels of Tm^{3+} for UC emissions. When Yb^{3+} absorbs a 976 nm photon and is excited to the $^2F_{5/2}$ level (GSA), the sequential ETs from Yb^{3+} to Er^{3+} (ET 1 and ET 3) populate the $^4F_{7/2}$ level of Er^{3+}, and the nonradiative relaxations then populate the states of $^2H_{11/2}$ and $^4S_{3/2}$. The radiative decays

Table 1. Quantum yields of the Er(Tm):YbAG and Er(Tm)-Mo:YbAG samples.

Sample	Average particle size [nm]	Power density [W cm^{-2}]	Quantum Yield [%]		
			Blue	Green	Red
Er:YbAG	48	20	–	0.000033	0.00037
Er-Mo:YbAG	57	20	–	0.2	0.01
Tm:YbAG	48	20	0.000017	0.0001	–
Tm-Mo:YbAG	56	20	0.18	–	–

$^2H_{11/2}\rightarrow^4I_{15/2}$ and $^4S_{3/2}\rightarrow^4I_{15/2}$ result in the green emissions. For the Tm:YbAG nanocrystals, three sequential ET processes from Yb^{3+} to Tm^{3+} result in the population of the $^1G_4$ state of Tm^{3+} (labeled ET 5, ET 6 and ET 7), followed by the blue emission $^1G_4\rightarrow^3H_6$.[3] However, due to strong lattice phonon couplings to the intermediate states of RE ions at the low energy level, the energy transferred from Yb^{3+} at the earliest stage of ET 1 for Er^{3+} or ET 5 for Tm^{3+} can relax to a lower energy level or be completely quenched; hence, the green and blue UC luminescence of Er^{3+} and Tm^{3+} becomes very dim, and the red UC emission takes place since the corresponding lower energy levels are populated, e.g. $^4F_{9/2}\rightarrow^4I_{15/2}$ for Er^{3+} and $^3F_2\rightarrow^3H_6$ for Tm^{3+}, resulting in red UC emissions as shown in Figure 2.[3] Furthermore, two nearby Yb^{3+} in $^2F_{5/2}$ level can form a coupled cluster state, which transfer their energy to Er^{3+} in $^4I_{15/2}$ and excite it to the $^4F_{7/2}$ level (ET 4), Tm^{3+} in $^3H_6$ and to the $^1G_4$ level (ET 8) respectively. However, ET 4 and ET 8 efficiencies are very low because the coupled cluster state is a virtual state.

The size of Er(Tm)-YbAG nanocrystals slightly increased with Mo addition. The larger nanocrystals with smaller surface ratio area causes lower probabilities of RE ions closer to the surface, which can enhance UC luminescence by decreasing nonradiative ET processes and surface quenching sites. However, the change of UC luminescence efficiency is limited by the variation of particle size from 30 to 100 nm.[11] Because the samples size increased about 8–9 nm by Mo co-doping, however, the green/blue UC luminescence efficiency increased about a four orders of magnitude, which indicated that the increase of samples size was not predominant factor in Er/Tm-Mo-Yb system.

Figure 4b shows our proposed UC mechanism for the Er(Tm)-Mo co-doped YbAG system. Unlike the cases without Mo co-doping, here the sensitization through the Yb^{3+}-MoO_4^{2-} dimer complex entails both GSA and ESA. The Yb^{3+}-MoO_4^{2-} dimer ground state is represented by $|^2F_{7/2}, ^1A_1>$, the intermediate excited state in the NIR by $|^2F_{5/2}, ^1A_1>$, and the relevant higher excited states by $|^2F_{7/2}, ^3T_1>$, $|^2F_{7/2}, ^3T_2>$, $|^2F_{7/2}$,
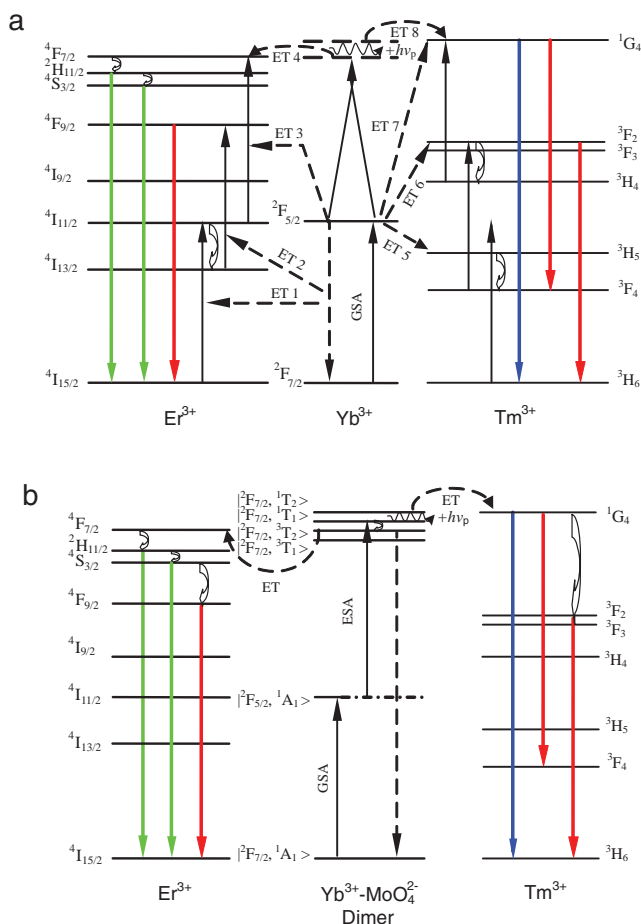
Figure 4. Sensitization diagrams. (a) Er(Tm)-Yb co-doped systems. (b) Er(Tm)-Yb-Mo co-doped systems.

$^1T_1>$, and $|^2F_{7/2}, ^1T_2>$, respectively. Here the GSA ($|^2F_{7/2}, ^1A_1>$ → $|^2F_{5/2}, ^1A_1>$) is followed by the ESA ($|^2F_{5/2}, ^1A_1>$ → $|^2F_{7/2}, ^1T_1>$). This combination of GSA+ESA is very similar to the recent finding in the Rb$_2$MnCl$_4$:Yb system.[13] However, unlike the Rb$_2$MnCl$_4$:Yb system where luminescence transition occurs within the Yb-Mn dimer, here the two-photon absorption is followed by a HESET to the Er(Tm) ions. In the case of Er^{3+}, the HESET from $|^2F_{7/2}, ^3T_2>$ state of the Yb^{3+}-MoO$_4$$^{2-}$ dimer to the $^4F_{7/2}$ level of Er^{3+} occurs, resulting in strong green UC luminescence. Similarly, in the Tm-Mo co-doped YbAG case, HESET from $|^2F_{7/2}, ^1T_2>$ state to the $^1G_4$ level of Tm^{3+} causes the strong blue emissions. Under this situation, it is also accompanied with phonon absorptions in order to compensate the tiny energy mismatch between the two-NIR-photon process and the emitted blue photon. The key feature here is that ET happens at much higher excited state energy in the Er(Tm)-Yb-Mo system than it does in the Er(Tm)-Yb system without Mo co-doping, which partly avoided the nonradiative decay processes happened at the lower energy levels of Er(Tm), leading to a great enhancement of green/blue UC emissions. The fact that the red emission in the Er(Tm)-Mo co-doped YbAG is more than two orders of magnitude weaker than the green-emission, as shown in Figure 2, provides further experimental evidence

for the proposed mechanism of the high excited state energy transfer UC process. The avoidance of phonon quenching via HESET process, as well as the exchange enhancement in the sensitization complex,[14] contribute to the extraordinary UC efficiency of green and blue emissions in Er(Tm)-Yb-Mo oxide materials.

Figure 5a shows the green UC emissions spectra for the Er-Mo:YbAG at the temperature of 295, 432, and 633 K. With the increase of temperature, the peak positions of green UC emissions at 522 and 546 nm have no change, however, the FIR of the two emissions varied. The energy gap of about 840 cm^{-1} between the $^2H_{11/2}$ and $^4S_{3/2}$ levels could be obtained from the green UC emissions spectra. This energy separation allows the $^2H_{11/2}$ level populated from $^4S_{3/2}$ level by thermal excitation and a quasi-thermal equilibrium occurs between the two levels, leading to variation in the transitions of $^2H_{11/2} \rightarrow ^4I_{15/2}$ and $^4S_{3/2} \rightarrow ^4I_{15/2}$ of Er^{3+} at the elevated temperature. With the thermalization of population at the two levels and ignoring the effects of self-absorption of the fluorescence, the FIR of green up-conversion emissions at 522 and 546 nm can be written as Equation (1).[15]

$$R \equiv \frac{I_{522}}{I_{546}} = \frac{N(^2H_{11/2})}{N(^4S_{3/2})} = \frac{g_H \sigma_H \omega_H}{g_S \sigma_S \omega_S} \exp\left[\frac{-\Delta E}{kT}\right]$$

$$= C \exp\left[\frac{-\Delta E}{kT}\right] \tag{1}$$

where I$_{522}$ and I$_{546}$ are the integrated intensity of the $^2H_{11/2} \rightarrow ^4I_{15/2}$ (520–540 nm) and $^4S_{3/2} \rightarrow ^4I_{15/2}$ (540–560 nm), respectively, N, g, σ, ω, are the number of ions, the degeneracy, the emission cross-section, the angular frequency of fluorescence transitions from the $^2H_{11/2}$, $^4S_{3/2}$ levels to $^4I_{15/2}$ level, respectively, ΔE the energy gap between the $^2H_{11/2}$ and $^4S_{3/2}$ levels, k the Boltzmann constant, T the absolute temperature, the pre-exponential constant is given by $C = g_H \sigma_H \omega_H / g_S \sigma_S \omega_S$.

Figure 5b shows a monolog plot of the FIR of green UC emissions at 522 and 546 nm as a function of inverse absolute temperature in the range of 295–973 K. The experimental data are fitted to straight line with the slope of about 900.8. The FIR of green up-conversion emissions at 522 and 546 nm relative to the temperature range of 295–973 K was shown in Figure 5c. The coefficient C value in Equation (1) is 8.82 according to fitting curve of the experimental data. The sensor sensitivity can be defined as Equation (2).[15]

$$\frac{dR}{dT} = R\left(-\frac{\Delta E}{kT^2}\right) \tag{2}$$

The corresponding resultant curve is shown in Figure 5d. At the temperature of 467 K, the sensitivity of Er-Mo:YbAG reached the maximal value of about 0.0048 K^{-1}. Several temperature cycles were performed and a good repeatability was obtained. Furthermore, there was no any modification in the sample and the green up-conversion emissions could be easily measured up to the highest temperature of 973 K, and a good repeatability was obtained with several temperature cycles. The temperature measurement resolution for the Er-Mo:YbAG was also relatively high, being about 0.3 K by employing a signal division circuitry with a precision of four digits or more.
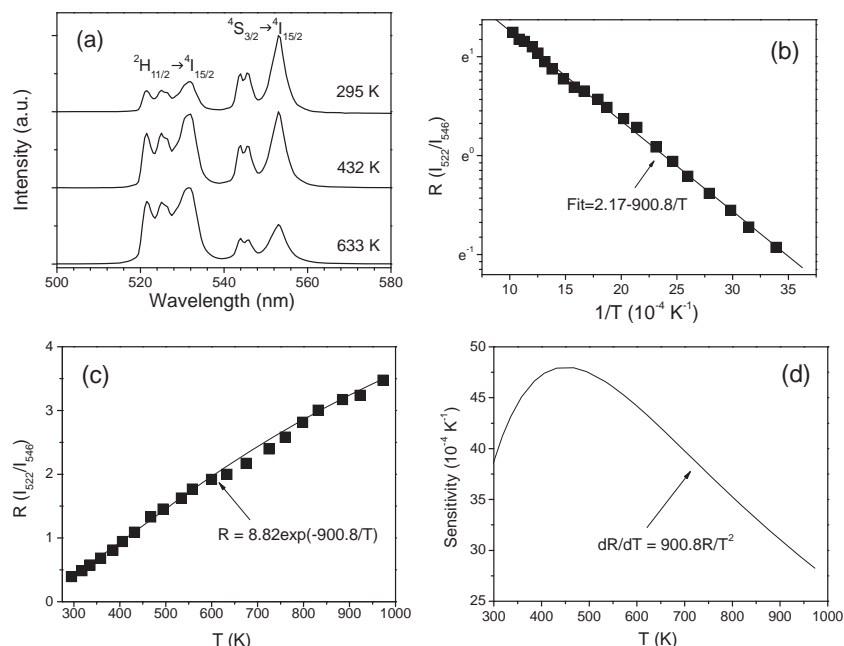
Figure 5. Temperature sensing based on the Er-Mo:YbAG. (a) green UC emissions spectra at different temperature, (b) monolog plot of the FIR as a function of inverse absolute temperature, (c) FIR relative to the temperature, (d) sensor sensitivity as a function of the temperature.

their high UC emissions efficiency. Although oxides have high chemical durability, thermal stability and mechanical strength, the application in in vivo imaging is still limited due to the low UC efficiency.

To demonstrate the feasibility of in vivo UC color imaging, we subcutaneously injected the poly acrylic acid (PAA) coated Er-Yb-Mo co-doped nanocrystals solutions into the back of nude mice, and then imaged them using the Maestro system with the 976 nm laser as the excitation light (power density ~0.2 W cm^{-2}). The localization of green colors at the point where the solution of PAA coated Er-Mo:YbAG nanocrystals was injected undoubtedly revealed the ability of Er-Mo:YbAG nanocrystals in multiplex in vivo imaging (**Figure 6**).

Here, we must note that Vetrone et al. for the first time realized optical sensing of temperature inside cells using the UC nanoparticles, and similar works were reported later, which would extend the fields of UC applications, such as in synthetic nanometer-sized structures and machines, temperature measurements in micro- and nanofluidic systems, in thermally induced drug release, and etc.[17] In 2011, Zhan et al. demonstrated that the 915 nm laser excitation method can achieve lager depth range in tissue and animal imaging, which successfully avoided the overheating effects with 980 nm excitation.[18]

In conclusion, we have demonstrated that the green/blue UC luminescence from Er(Tm)-Yb-Mo systems can be about four orders of magnitude more efficient than in the Er(Tm)-Yb systems without Mo co-doping. Such high efficiency is due to a novel HESET pathway in Er(Tm)-Yb-Mo systems that is completely different from the normal energy transfer route at lower energy (NIR) level, thus partly avoided the phonon quenching processes and significantly enhanced the UC emissions of oxide based materials. With this obstacle is overcome, one can utilize the advantageous material properties of oxides and the highly efficient UC luminescence of

The optical temperature sensing ability of other RE doped material is shown in **Table 2**.[15] Compared with various oxide, fluoride matrix and hybrid nanoparticles, a favorable result was achieved in the Er-Mo:YbAG. The Er-Mo:YbAG with operating temperature range (295–973 K), temperature measurement resolution (0.3 K) and excitation power (2 mW) indicated that it is more promising for applications in the temperature sensing.

UC nanocrystals have been considered as a new class of fluorescent probes for in vivo imaging in recent years.[16] Compared with organic dyes, fluorescent proteins and quantum dots, UC nanocrystals appear obvious advantages in the field of in vivo imaging, including improvement of the signal-to-noise ratio, increase of tissue penetration, decrease of photo-bleaching and photo-toxicity.[16] Up to date, reports of in vivo imaging concentrate mainly on the Er-Yb co-doped fluorides because of

Table 2. Summarized performance of RE ions doped materials as temperature sensing elements.

| Phosphor	Temperature Range [K]	Excitation Power [mW]/Excitation source [nm]	Maximum Sensitivity [K^{-1}]	Resolution [K]
Er-Mo:Yb$_3$Al$_5$O$_{12}$	295–973	2/976	0.0048	0.3
Er-Yb:Gd$_2$O$_3$	300–900	280/976	0.0039	
Er:BaTiO$_3$	322–466	2000 W cm^{-2}/980	0.0052	
Er:SiO$_2$	295–873	200/800	0.001	1.3
Er-Yb:Al$_2$O$_3$	295–973	350/978	0.0051	0.3
Er-Yb:fluoride glass	296–448	5/1480	0.004	1
Er/Er-Yb:chalcogenide glass	293–498	150/1060	0.0052	0.5
Eu hybrid NPS	283–323	—/405	0.031	0.1
Eu-Tb hybrid NPS	10–350	—/365	0.047	
Eu-Tb complexes	273–343	1/405	0.012	0.1
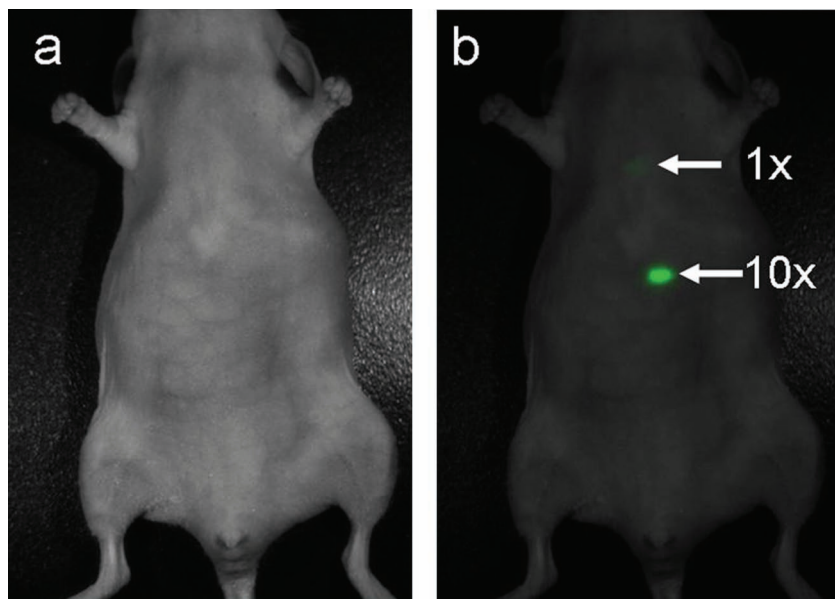
Figure 6. Images of a mouse injected with solutions of PAA coated Er-Mo:YbAG nanocrystals. (a) Bright field image, (b) Fluorescent images (1x: 0.01 mg mL^{-1}, 10x: 0.1 mg mL^{-1}).

Er(Tm)-Yb-Mo systems for a wide range of applications, such as temperature sensing and in vivo imaging. Moreover, this novel mechanism would stimulate further discovery of other UC RE materials with the designed material and optical functionalities.

Experimental Section

Synthesis of RE oxide nanoparticles: Er-Mo, Tm-Mo co-doped YbAG nanocrystals with nominal compositions of Er$_{0.25}$Yb$_{2.25}$Mo$_{0.5}$Al$_5$O$_{12}$ (Er-Mo:YbAG) and Tm$_{0.25}$Yb$_{2.25}$Mo$_{0.5}$Al$_5$O$_{12}$ (Tm-Mo:YbAG) were prepared via the sol-gel method; Er- or Tm-doped YbAG nanocrystals with nominal compositions of Er$_{0.25}$Yb$_{2.75}$Al$_5$O$_{12}$ (Er:YbAG) and Tm$_{0.25}$Yb$_{2.75}$Al$_5$O$_{12}$ (Tm:YbAG) were made by the same method for comparison. The detailed synthesis procedure was as following: Al(OC$_3$H$_7$)$_3$ was first added into the acetylacetone and isopropanol solution with a concentration of 2 mol L^{-1}, ranging a molar ratio of 1:2 between Al(OC$_3$H$_7$)$_3$ and acetylacetone. After aging for 1 h, hydrolysis of the modified precursor was performed in a isopropanol environment with a concentration of Al(OC$_3$H$_7$)$_3$ of 30 g L^{-1} and a molar ratio of 0.85:1 between water and Al(OC$_3$H$_7$)$_3$. The resulting solution was agitated for 3 h, and then the pH value was adjusted to about 3.0 with HNO$_3$, forming a clear, slightly yellow and very stable Al$_2$O$_3$ sol. Finally, Er(Tm), Mo and Yb were introduced by adding Er(NO$_3$)$_3$·5H$_2$O(or Tm(NO$_3$)$_3$·5H$_2$O), (NH$_4$)$_6$Mo$_7$O$_{24}$·4H$_2$O and Yb(NO$_3$)$_3$·5H$_2$O with a molar ratio of 0.25:x:2.75-x:5 (x = 0, 0.5) for Er(Tm):Mo:Yb:Al. x = 0 means no Mo co-doping. The sols were dried at 373 K to remove the solvent, and the xerogels obtained were annealed at 1523 K for 1 h and then cooled down to room temperature in the furnace.

Elemental analysis: The molar ratios of Er(Tm):Yb and Er(Tm):Mo:Yb of the UC nanocrystals were obtained by X-ray fluorescence (X2F-1800) (Supporting information).

Structure analysis: Structural and phase purity characterizations were carried out by powder X-ray diffraction (XRD) using a Shimadzu XRD-6000 diffractometer with Cu Kα radiation. TEM investigations were performed on a Tecnai F20 (200 kV) electron microscope.

Spectra and quantum yield measurement of room temperature: The dried RE oxide nanoparticles were filled in a quartz cuvette with a width of 1 mm. A 976 nm semiconductor laser diode (LD) illuminated the sample at an angle about 15° from the normal direction of one side of the cuvette, and the UC emission was measured by an iHR 550 spectrometer with spectral resolution of 0.1 nm, in a back scattering configuration normal to the illuminated side of the cuvette. Spectra measurements were performed under the identical conditions, such as the position of the sample, excitation source (excitation power and focusing spot), slits aperture and the detection performance. Refer to the method provided by Chen et al., the quantum yields of the samples were measured with the Er-Yb:NaYF$_4$ material (with quantum yield of 4% for the green UC luminescence by 976 nm excitation) as the reference sample.[19] All the measurements were carried out at room temperature.

Spectra measurement of high temperature: The sample (Er-Mo:YbAG nanocrystals were pressed into thin pieces with dimensions of 5 mm × 5 mm × 0.2 mm) was placed in a furnace and its temperature increased from 295 to 973 K (the highest temperature of the furnace) with measurement error of ±1.5 K was monitored by a copper-constantan thermocouple set to the back-face of sample. The green UC emission spectra in the wavelength range of 500–580 nm were detected from the sample using a 976 nm LD with excitation power of 2 mW. The green UC emission from the sample was measured by an iHR 550 spectrometer with spectral resolution of 0.1 nm.

Synthesis of PAA coated Er-Mo:YbAG nanocrystals: Water-soluble Er-Mo:YbAG nanocrystals were prepared by a hydrothermal process. Typically, 5 mg of Er-Mo:YbAG nanocrystals, 10 mg of PAA (MW = 1800 Da, Sigma-Aldrich) and 10 mL of distilled water were mixed together under bath sonication to form a suspension, which was then transferred to a 18 mL autoclave, sealed and then heated at a designed temperature of 413 K for approximately 6 h. The system was cooled to room temperature naturally and most of the water-soluble product was in the supernatant solution. The supernatant was collected and centrifuged at 14000 rpm for 5 min. The final product was at the bottom of the tube and could be easily redispersed in aqueous solutions.

Animal experiments and in vivo imaging: Athymic nude mice experiments were obtained from Suzhou Belda Bio-Pharmaceutical Co. and performed under protocols approved by Soochow University Laboratory Animal Center.

For subcutaneous injection and UC imaging, the PAA coated Er-Mo:YbAG nanocrystals aqueous solutions (15 µL, 0.01–0.1 mg mL^{-1}) in a 0.9% NaCl saline solution were subcutaneously injected into the back area of nude mice. Mice were then imaged by a Maestro in vivo fluorescent imaging system (CRi Inc.) using a 976 nm optical fiber-coupled laser as the excitation source. The laser power density was ~0.2 W cm^{-2} during imaging, which was classified as a safe power according to previous in vivo photothermal therapy studies. An 850 nm short-pass emission filter was applied to prevent the interference of excitation light with the CCD camera. The exposure time was 2 s per frame. Mice were anaesthetized by isoflurane during imaging.

Modelling: The first-principles calculations are performed within the framework of density functional theory (DFT), employing the VASP package.[20] We use projector-augmented-wave pseudopotentials[21] to describe the electron-nucleus interaction and the PBE formulation[22] for the exchange-correlation functional, which are the most reliable in describing structural and electronic properties of bulk materials. For simplicity the experimental lattice constant of Yb$_3$Al$_5$O$_{12}$, a = 11.939 Å, is used and the unit cell contains 24 Yb, 40 Al and 96 O atoms for the perfect crystal. A plane wave cutoff of 400 eV and a single k-point are employed. Energy eigenvalue smearing at the Fermi level is utilized with a Gaussian width of 0.2 eV. All atoms in the cell including substitutional dopants are allowed to relax. Geometrical optimization is stopped when the forces on all the atoms are less than 0.05 eV Å^{-1}. These computational parameters ensure an accuracy

[1] a) F. Auzel, *C. R. Acad. Sci. (Paris)* **1966**, *262*, 1016; b) F. Auzel, *C. R. Acad. Sci. (Paris)* **1966**, *263B*, 819.

[2] a) S. Sivakumar, F. C. J. M. van Veggel, M. Raudsepp, *J. Am. Chem. Soc.* **2006**, *128*, 2115; b) X. Wang, X. G. Liu, *J. Am. Chem. Soc.* **2008**, *130*, 5642; c) H. R. Zheng, X. J. Wang, M. J. Dejneka, W. M. Yen, R. S. Meltzer, *J. Lumin.* **2004**, *108*, 395; d) Z. Q. Li, Y. Zhang, S. Jiang, *Adv. Mater.* **2008**, *20*, 4765; e) R. Naccache, F. Vetrone, V. Mahalingam, L. A. Cuccia, J. A. Capobianco, *Chem. Mater.* **2009**, *21*, 717; f) F. Auzel, *Chem. Rev.* **2004**, *104*, 139; g) J. F. Suyver, A. Aebischer, D. Biner, P. Gerner, J. Grimm, S. Heer, K. W. Krämer, C. Reinhard, H. U. Güdel, *Opt. Mater.* **2005**, *27*, 1111.

[3] a) R. Naccache, F. Vetrone, V. Mahalingam, L. A. Cuccia, J. A. Capobianco, *Chem. Mater.* **2009**, *21*, 717; b) J. C. Boyer, L. A. Cuccia, J. A. Capobianco, *Nano Lett.* **2007**, *7*, 847; c) R. Balda, J. Fernández, A. Mendioroz, M. Voda, M. Al-Saleh, *Phys. Rev. B* **2003**, *68*, 165101.

[4] M. J. Dejneka, A. Streltsov, S. Pal, A. G. Frutos, C. L. Powell, K. Yost, P. K. Yuen, U. Müller, J. Lahiri, *PANS* **2003**, *100*, 389.

[5] a) K. W. Krämer, D. Biner, G. Frei, H. U. Güdel, M. P. Hehlen, S. R. Lüthi, *Chem. Mater.* **2004**, *16*, 1244; b) G. F. Wang, Q. Peng, Y. D. Li, *J. Am. Chem. Soc.* **2009**, *131*, 14200; c) P. Li, Q. Peng, Y. D. Li, *Adv. Mater.* **2009**, *21*, 1945.

[6] a) F. Wang, Y. Han, C. S. Lim, Y. H. Lu, J. Wang, J. Xu, H. Y. Chen, C. Zhang, M. H. Hong, X. G. Liu, *Nature* **2010**, *463*, 1061; b) J. C. Boyer, L. A. Cuccia, J. A. Capobianco, *Nano Lett.* **2007**, *7*,

[7] S. A. Wade, S. F. Collins, G. W. Baxter, *J. Appl. Phys.* **2003**, *94*, 4743.

[8] B. S. Cao, Y. Y. He, Z. Q. Feng, Y. S. Li, B. Dong, *Sens. Actuators B* **2011**, *159*, 8.

[9] a) M. Kaczkan, M. Borowska, K. Kolodziejak, T. Lukasiewicz, M. Malinowski, *Opt. Mater.* **2008**, *30*, 703; b) Y. S. Wu, J. Li, Y. B. Pan, Q. Liu, J. K. Guo, *Ceram. Int.* **2009**, *35*, 25.

[10] B. Etschmann, V. Streltsov, N. Ishizawa, E. N. Maslen, *Acta Crystallogr. B* **2001**, *57*, 136.

[11] J. C. Boyer, F. C. J. M. van Veggel, *Nanoscale* **2010**, *2*, 1417.

[12] M. Pollnau, D. R. Gamelin, S. R. Lüthi, H. U. Güdel, M. P. Hehlen, *Phys. Rev. B* **2000**, *61*, 3337.

[13] a) C. Reinhard, R. Valiente, H. U. Güdel, *J. Phys. Chem. B* **2002**, *106*, 10051; b) P. Gerner, C. Reinhard, H. U. Güdel, *Chem. Eur. J.* **2004**, *10*, 4735.

[14] Y. Tanabe, T. Moriya, S. Sugano, *Phys. Rev. Lett.* **1965**, *15*, 2023.

[15] a) S. K. Singh, K. Kumar, S. B. Rai, *Sens. Actuators A* **2009**, *149*, 16; b) M. A. R. C. Alencar, G. S. Maciel, C. B. de Araujo, *Appl. Phys. Lett.* **2004**, *84*, 4753; c) E. Maurice, G. Monnom, B. Dussardier, A. Saissy, D. B. Ostrowsky, G. W. Baxter, *Appl. Opt.* **1995**, *34*, 8019; d) B. Dong, D. P. Liu, X. J. Wang, T. Yang, S. M. Miao, C. R. Li, *Appl. Phys. Lett.* **2007**, *90*, 181117; e) G. S. Maciel, L. de S. Menezes, A. S. L. Gomes, C. B. de Araujo, Y. Messaddeq, A. Florez, M. A. Aegerter, *IEEE Photonic Tech. Lett.* **1995**, *7*, 1474; f) P. V. dos Santos, M. T. de Araujo, A. S. Gouveia-Neto, J. A. Medeiros Neto, A. S. B. Sombra, *IEEE J. Quantum Electron.* **1999**, *35*, 395; g) H. S. Peng, S. H. Huang, O. S. Wolfbeis, *J. Nanopart. Res.* **2010**, *12*, 2729; h) C. D. S. Brites, P. P. Lima, N. J. O. Silva, A. Millán, V. S. Amaral, F. Palacio, L. D. Carlos, *Adv. Mater.* **2010**, *22*, 4499; i) H. S. Peng, M. I. J. Stich, J. B. Yu, L. N. Sun, L. H. Fischer, O. S. Wolfbeis, *Adv. Mater.* **2010**, *22*, 716; j) J. B. Yu, L. N. Sun, H. S. Peng, M. I. J. Stich, *J. Mater. Chem.* **2010**, *20*, 6975.

[16] a) D. E. Achatz, R. Ali, O. S. Wolfbeis, *Top Curr. Chem.* **2011**, *300*, 29; b) H. S. Mader, P. Kele, S. M. Saleh, O. S. Wolfbeis, *Curr. Opin. Chem. Biol.* **2010**, *14*, 582; c) J. Zhou, Z. Liu, F. Y. Li, *Chem. Soc. Rev.* **2012**, *41*, 1323.

[17] a) F. Vetrone, R. Naccache, A. Zamarron, A. J. de la Fuente, F. Sanz-Rodriguez, L. M. Maestro, E. M. Rodriguez, D. Jaque, J. G. Sole, J. A. Capobianco, *ACS Nano* **2010**, *4*, 3254; b) L. H. Fisher, G. S. Harms, O. S. Wolfbeis, *Angew. Chem. Int. Ed.* **2011**, *50*, 4546; c) C. D. S. Brites, P. P. Lima, N. J. O. Silva, A. Millán, V. S. Amaral, F. Palacio, L. D. Carlos, *New J. Chem.* **2011**, *35*, 1177.

[18] Q. Q. Zhan, J. Qian, H. J. Liang, G. Somesfalean, D. Wang, S. L. He, Z. G. Zhang, S. A. Engels, *ACS Nano* **2011**, *5*, 3744.

[19] G. Y. Chen, T. Y. Ohulchanskyy, A. Kachynski, H. Agren, P. N. Prasad, *ACS Nano* **2011**, *6*, 4981.

[20] G. Kresse, J. Hafner, *Phys. Rev. B* **1993**, *47*, 558.

[21] P. E. Blochl, *Phys. Rev. B* **1994**, *50*, 17953.

[22] J. P. Perdew, K. Burke, M. Ernzerhof, *Phys. Rev. Lett.* **1996**, *77*, 3865.